Multi-material ALE computation using the radiation hydrodynamic code CHIC

Chapter · January 2020

1 author:

Jérôme Breil
Atomic Energy and Alternative Energies Commission
106 PUBLICATIONS   **2,713** CITATIONS

Chapter 4

Multi-material ALE computation using the radiation hydrodynamic code CHIC

In ICF a high power laser compress a spherical capsule to a high density and temperature hot spot in order to ignite a thermonuclear burn. During this compression process we have to deal with large displacements and strong shocks. Spherical capsule used in ICF are usually the assembly of multi-material layers. For numerical purpose and with regards to the large volume change, Lagrange formulation is well adapted to compute such problems. As the mesh moves with the fluid it handles naturally the interface between different materials and the large displacement during the compression of the target. One of the critical issue in direct drive ICF is the sensibility to hydrodynamics instabilities especially to Rayleigh-Taylor instability at the interface between the different materials during stagnation phase [97]. To deal with such problems pure Lagrange frame suffers from a lack of robustness. When such instabilities occur large distortions of the mesh can lead to tangled cells. A commonly used alternative is to consider an Arbitrary Lagrangian Eulerian (ALE) formulation [76]. A pure Lagrangian phase is followed by a two-step process: the rezoning of the Lagrangian mesh followed by a remapping step.

In this context of multi-material computation using the Full-ALE method as interface is modified by the rezoning, mixed cells containing several materials may appear. These mixed cells contain material interfaces, which need special treatment to be taken into account. In our strategy, this is done using the MOF method presented in section 2.2. Furthermore, a closure model is applied in the way to determinate the evolution of the volume fraction and the thermodynamic state of each material using real equations of state (EOS) during the Lagrangian steps. We have developed such a strategy in the 2D CHIC (Code d'Hydrodynamique d'Implosion du CELIA) code [33] which is based on a cell-centered discretization of Lagrangian hydrodynamic to simulate ICF and plasma physics experiment created by laser interaction with target.

This Chapter is organized as follows. We first briefly describe the coupling of the numerical methods. Then, theoretical and experimental studies from [37, 115, 74, 129, 19] are given to highlight the robustness and accuracy of the CHIC code.

4.1 Physical model of CHIC code

CHIC is a 2D ALE integrated ICF code developed at CELIA. This code is currently used to simulate ICF studies [146, 136, 74, 129, 126]. The code includes two-dimensional Lagrangian hydrodynamics in planar and cylindrical geometry, ion and classical or non-local electron heat
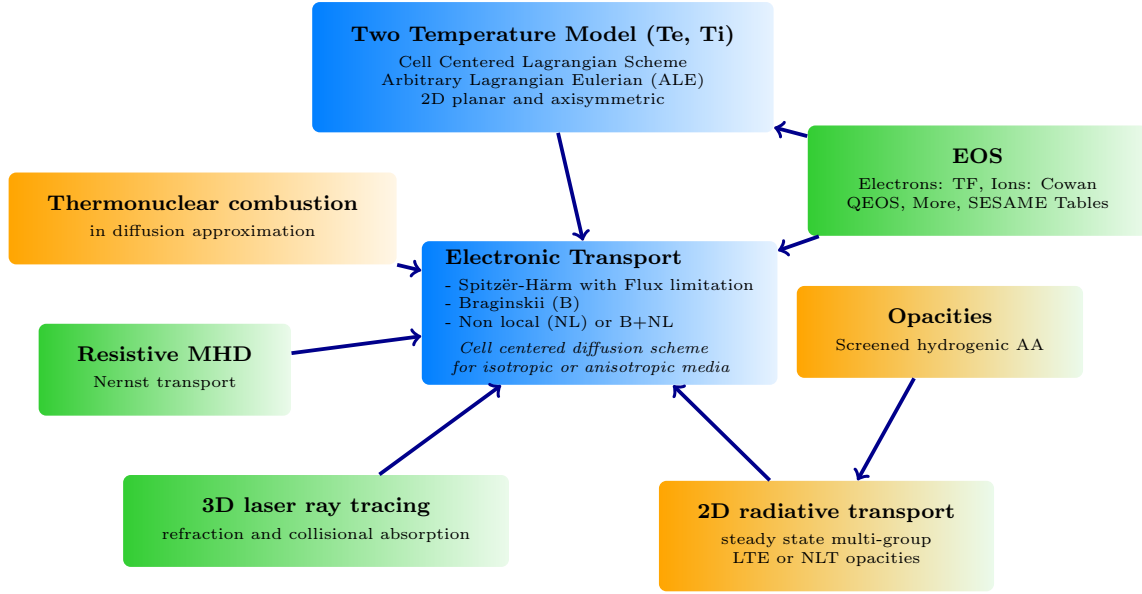
Figure 4.1: CHIC main packages

conduction, thermal coupling of electrons and ions and a detailed radiation transport. The ALE method is implemented to improve the geometrical quality of the grid elements and to optimize accuracy, robustness and computational efficiency [32, 65]. The ionization and the opacity data are tabulated, assuming a local thermodynamic equilibrium (LTE) or a non-LTE depending on the plasma parameters. The radiative transport is computed assuming that the radiation field is quasistationary and weakly anisotropic with regards to angular dependency (multigroup diffusion). The equations of state implemented in the code are QEOS and SESAME. The laser propagation, refraction and collisional absorption are treated by a ray tracing algorithm. A resistive Magnetohydrodynamics (MHD) package accounting for the azimuthal magnetic fields generated by the thermal sources (crossed gradients of the density and the electron temperature) is also included. As we can see on FIG. 4.1 all the different physical model are strongly coupled to the hydrodynamics model. The plasma fluid model in Lagrangian formalism writes as

$$\rho\frac{d\tau}{dt} - \nabla \cdot \boldsymbol{U} = 0,$$

$$\rho\frac{d\boldsymbol{U}}{dt} + \boldsymbol{\nabla}(P_{\mathrm{i}} + P_{\mathrm{e}}) = \boldsymbol{0},$$

$$\rho\left(\frac{d\varepsilon_{\mathrm{e}}}{dt} + P_{\mathrm{e}}\frac{d\tau}{dt}\right) - \nabla \cdot (\lambda_{\mathrm{e}}\boldsymbol{\nabla}T_{\mathrm{e}}) = \Omega_{\mathrm{ei}}(T_{\mathrm{i}} - T_{\mathrm{e}}) + W_{\mathrm{las}} + W_{\mathrm{rad}} + W_{\mathrm{fus}},$$

$$\rho\left(\frac{d\varepsilon_{\mathrm{i}}}{dt} + P_{\mathrm{i}}\frac{d\tau}{dt}\right) = \Omega_{\mathrm{ei}}(T_{\mathrm{e}} - T_{\mathrm{i}}).$$

Here ρ denotes the density, $\tau = \frac{1}{\rho}$, $\boldsymbol{U}$ the velocity, P_{i} and P_{e} are the ion and electron pressures, ε_{i} and ε_{e} are the specific internal energies for ion and electron and T_{i} and T_{e} are the ion and electron temperatures. We introduce Ω_{ei} which is an exchange energy term between ion and electron and λ_{e} is the conductivity coefficient for electron transport. W_{las}, W_{rad} and W_{fus} are respectively the source term for laser, radiative transport and nuclear fusion.

The thermodynamic closure of this system is given by the equation of state (EOS), $P_{\mathrm{e}} \equiv \mathcal{P}_{\mathrm{e}}(\rho, T_{\mathrm{e}})$, $P_{\mathrm{i}} \equiv \mathcal{P}_{\mathrm{i}}(\rho, T_{\mathrm{i}})$, $\varepsilon_{\mathrm{e}} \equiv \epsilon_{\mathrm{e}}(\rho, T_{\mathrm{e}})$ and $\varepsilon_{\mathrm{i}} \equiv \epsilon_{\mathrm{i}}(\rho, T_{\mathrm{i}})$.

4.1.1 Numerical methods

In the context of multi-material ALE computation, as grid and fluid move separately mixed cells containing material interface appear. A number of numerical methods exist for taking into account such interface. Here we use the MOF method presented in section 2.2. A closure model is also required to define how the thermodynamic states of the multi-material cells evolve during the Lagrangian and the remapping phases [22]. In this work, we will use an homogeneous model for the temperature and we will set only one temperature for the ion and electron such that each material will have the same ion and electron temperature in a mixed cell. Finally, we will need closure model for all the different physical quantities that are usually material dependent.

4.1.2 Lagrangian phase

In Lagrangian hydrodynamics methods, a computational cell moves with the flow velocity its mass being time-invariant. Thus, Lagrangian methods can capture contact discontinuity sharply in multi-material fluid flows. Here the Lagrangian scheme is based on a cell-centered discretization of Lagrangian hydrodynamics equations [113]. This scheme is written in total energy form.

$$\rho \frac{d\tau}{dt} - \nabla \cdot \boldsymbol{U} = 0,$$

$$\rho \frac{d\boldsymbol{U}}{dt} + \boldsymbol{\nabla} P = \boldsymbol{0},$$

$$\rho \frac{dE}{dt} + \nabla \cdot \boldsymbol{P}\,\boldsymbol{U} = 0.$$

Where $P = P_{\mathrm{i}} + P_{\mathrm{e}}$ is the total pressure and E the total energy. The accuracy in space is improved thanks to a second-order extension which uses the piecewise linear monotone reconstruction of the pressure and velocity. The piecewise linear monotone reconstruction is achieved using a least squares procedure followed by a slope limitation procedure. The time discretization is a one step high order extension based on the acoustic generalized Riemann problem. This high-order Lagrangian scheme is precisely described in [114].

4.1.3 Two-temperature model

Based on total energy conservation, the Lagrangian scheme must deal with the exchange between the kinetic energy and the internal energy of ion and electron. The system we want to solve for the internal energy of ion and electron is

$$\rho \left(\frac{d\varepsilon_{\mathrm{e}}}{dt} + P_{\mathrm{e}} \frac{d\tau}{dt} \right) - \nabla \cdot (\lambda_{\mathrm{e}} \boldsymbol{\nabla} T_{\mathrm{e}}) = \Omega_{\mathrm{ei}}(T_{\mathrm{i}} - T_{\mathrm{e}}),$$

$$\rho \left(\frac{d\varepsilon_{\mathrm{i}}}{dt} + P_{\mathrm{i}} \frac{d\tau}{dt} \right) = \Omega_{\mathrm{ei}}(T_{\mathrm{e}} - T_{\mathrm{i}}).$$

We will compute the new ion and electron internal energy in two steps. First, after the Lagrangian step we have a new internal energy which is the sum of ion and electron internal energy. To compute the electron internal energy we make the assumption that the entropy deposition is done on the ion internal energy [168]. Thus, electrons follow the isentropic evolution

$$m \frac{d\,\varepsilon_{\mathrm{e}}}{dt} + P_{\mathrm{e}} \frac{d\,V}{dt} = 0.$$

Where $m = \rho\,V$ is the mass and V the volume. We can deduce ion internal energy from

$$\varepsilon_{\mathrm{i}} = \varepsilon - \varepsilon_{\mathrm{e}}$$

97

Where $\varepsilon = E - \frac{1}{2}\boldsymbol{U}^2$ is the mean internal energy. Then, to solve the non linear conduction and the energy transfer between ion and electron we use a Newton algorithm. The system we solve in this step is equivalent to

$$\rho\frac{d\varepsilon_{\mathrm{e}}}{dt} - \nabla \cdot (\lambda_{\mathrm{e}}\boldsymbol{\nabla}T_{\mathrm{e}}) = \Omega_{\mathrm{ei}}(T_{\mathrm{i}} - T_{\mathrm{e}}),$$
$$\rho\frac{d\varepsilon_{\mathrm{i}}}{dt} = \Omega_{\mathrm{ei}}(T_{\mathrm{e}} - T_{\mathrm{i}}).$$

Here λ_{e} is the Spitzer-Härm thermal conductivity which is proportional to $\approx T_{\mathrm{e}}^{\frac{5}{2}}$. The diffusion operator is discretized using a numerical scheme [36, 115] which is a second order cell centered finite volume scheme that can be applied to unstructured mesh. It is a robust and accurate scheme well adapted to distorted mesh.

At that time we need to update pressure using EOS as temperature field has been modified. Due to the electron transport modelized by the diffusion term we also need to update the mean internal energy and total energy

$$\varepsilon = \varepsilon_{\mathrm{i}} + \varepsilon_{\mathrm{e}},$$
$$E = \varepsilon + \frac{1}{2}\boldsymbol{U}^2.$$

4.1.4   Thermodynamical closure for the multi-material cells

A closure model is required to define how the thermodynamic states of the multi-material cells evolve during the Lagrangian and the remapping steps. The model we use is based on the reconstruction of the material interface inside a mixed cell, in which, each material evolves separately. The goal here is to compute, using the partial quantities, the mean pressure and sound speed using the quantities of every material. Let ϕ_k be the volume fraction defined for the fluid k in a cell by $\phi_k = \frac{V_k}{V}$, where V_k is the volume of the cell's part occupied by the fluid k and V the volume of the cell. Using Gibbs relation applied to the mean fluid, the pressure of the mean fluid is obtained

$$P = \sum_k \phi_k P_k.$$

Concerning the sound speed, we obtain

$$c^2 = \sum_k \frac{m_k}{m} c_k^2.$$

We make now the assumption that we have only one electron and one ion temperature for each material per mixed cells. We define the mean conductivity, using harmonic mean

$$\lambda_{\mathrm{e}} = \frac{\displaystyle\sum_k \phi_k}{\displaystyle\sum_k \frac{\phi_k}{\lambda_{\mathrm{e},k}}}.$$

Harmonic mean is usually used when a mean conductivity is required for example at the interface between two materials. For the exchange energy term between ion and electron we use arithmetic mean

$$\Omega_{\mathrm{ei}} = \sum_k \phi_k \Omega_{\mathrm{ei,k}}.$$

4.2 Modelling of the magnetic field effects using tensorial diffusion

This work is part of a collaboration we had with the Institute of Laser Engineering (ILE) at Osaka University where I was invited to work on the coupling of such magnetic field with the plasma [124]. In laser generated plasmas, magnetic fields are created whenever density and temperature gradients are not colinear. Dedicated experiments and numerical computations evidenced fields in the 100 kG-1MG range in plasmas typical of laser driven ICF [146, 126, 6]. As the corresponding magnetic pressure stays far below the kinetic pressure, the hydrodynamic flow is not directly altered by such fields. Conversely, the electron gyrofrequency is comparable to the electron-ion collision frequency in the vicinity of the critical density region, which may affect dramatically the electron heat flow. Key issues of ICF are laser matter coupling, mass ablation, hydrodynamic instabilities and hot spot dynamics. Because all of these phenomena are highly sensitive to electron heat transport, accurate modelling of the electron conduction is an essential ingredient of numerical simulations. However, the electron conduction model implemented in the majority of hydrodynamic codes is based upon the flux limited Spitzer-Härm theory and does not account for magnetic fields. The classical formulas by Braginskii predict that magnetic fields provide a reduction of the magnitude of the heat flux and its rotation through the Righi-Leduc effect. Splitting the Righi-Leduc term or approximating it as an advection term or an effective conductivity often leads to mathematical and physical anomalies. Alternatively, a direct space differencing of the full conduction operator raises accuracy and consistency issues. We developed in CELIA a new, fully tensorial approach which overcomes these difficulties. We propose a new second order tensorial diffusion method which is based on a cell-centered diffusion scheme [115]. We present the main idea of the space differencing scheme and some numerical results that illustrate the efficiency of the method compared to standard approaches. The packages describing the magnetic field generation and the anisotropic electron heat transport have been incorporated in the hydrodynamic code CHIC.

4.2.1 Underlying physical models

In deriving a numerical method to solve the heat conduction equation (3.1), we aim at developing numerical modeling of physical phenomena encountered in plasma physics. More precisely, we are concerned by heat transfer within laser-heated plasma flows such as those obtained in the domain of direct drive Inertial Confinement Fusion, refer to [13]. In this context, the energy released by the laser is transferred throughout the plasma flows by means of electron heat conduction. Omitting the pressure work term, which results from coupling to hydrodynamics, the electron temperature, T_e, is governed by a heat conduction equation similar to (3.1). In the classical regime, the electron heat flux, q_e is given by the Spitzer-Härm law: $q_e = -\kappa_e \boldsymbol{\nabla} T_e$, where the electron thermal conductivity, κ_e, depends on the electron temperature as a power law, *i.e.*, $\kappa_e(T_e) \sim T_e^{\frac{5}{2}}$, refer to [51, 168]. This corresponds to an isotropic nonlinear heat conduction equation. However, in presence of magnetic fields, this isotropic model for heat conduction is not valid anymore. Such a situation occurs frequently for laser driven plasma wherein the density and pressure gradients are not colinear. In this particular case, a self-generated magnetic field, $\boldsymbol{B}$, is created by the rotational component of the ambipolar electric field, $\boldsymbol{E} = -\frac{1}{eN_e} \boldsymbol{\nabla} P_e$, where e is the electron charge, N_e is the electron density per unit volume and P_e is the electron pressure, refer to [51]. Knowing that the magnetic field is governed by the Faraday law, *i.e.*, $\frac{\partial \boldsymbol{B}}{\partial t} + \boldsymbol{\nabla} \times \boldsymbol{E} = \boldsymbol{0}$, we deduce that the time evolution of the magnetic field

is governed by the following equation

$$\frac{\partial \boldsymbol{B}}{\partial t} = \frac{1}{e}\boldsymbol{\nabla}(\frac{1}{N_e}) \times \boldsymbol{\nabla} P_e. \tag{4.1}$$

The magnetic field dramatically modifies electron heat transport leading to a anisotropic electron conductivity. It implies not only a reduction of the magnitude of the heat flux but also its rotation. Using plasma kinetic theory, Braginskii [30] has obtained the following expression of the electron heat flux with magnetic field

$$\boldsymbol{q}_e = -\kappa_\parallel(\boldsymbol{\nabla} T_e \cdot \boldsymbol{b})\boldsymbol{b} - \kappa_\perp[\boldsymbol{\nabla} T_e - (\boldsymbol{\nabla} T_e \cdot \boldsymbol{b})\boldsymbol{b}] - \kappa_\wedge \boldsymbol{b} \times \boldsymbol{\nabla} T_e, \tag{4.2}$$

where $\boldsymbol{b} = \frac{\boldsymbol{B}}{|\boldsymbol{B}|}$ is unit vector corresponding to the direction of the magnetic field and $\kappa_\parallel$, $\kappa_\perp$ and $\kappa_\wedge$ are scalar conductivities given in [30]. Let us consider a two-dimensional plasma flow in planar geometry. Let $(\boldsymbol{e}_x, \boldsymbol{e}_y, \boldsymbol{e}_z)$ be the orthonormal basis of $\mathfrak{R}^3$ and suppose that the two-dimensional flow is contained in the frame (x, y) equipped with the orthonormal basis $(\boldsymbol{e}_x, \boldsymbol{e}_y)$. By virtue of (4.1), it is obvious that the self-generated magnetic field is transverse to the two-dimensional flow, that is, $\boldsymbol{B} = B\boldsymbol{e}_z$. Setting $b = \frac{B}{|B|}$, we have $\boldsymbol{b} = b\boldsymbol{e}_z$, where $b^2 = 1$. Bearing this in mind, the electron heat flux expression (4.2) collapses to

$$\boldsymbol{q}_e = -\kappa_\perp \boldsymbol{\nabla} T_e - \kappa_\wedge \boldsymbol{b} \times \boldsymbol{\nabla} T_e. \tag{4.3}$$

Developing the above equation over the Cartesian frame (x, y) allows to write the electronic heat flux

$$\boldsymbol{q}_e = -\mathsf{K}_e \boldsymbol{\nabla} T_e, \tag{4.4}$$

where the second-order tensor K_e corresponds to the electronic conductivity defined by

$$\mathsf{K}_e = \begin{pmatrix} \kappa_\perp & -b\kappa_\wedge \\ b\kappa_\wedge & \kappa_\perp \end{pmatrix}. \tag{4.5}$$

The Braginskii transport coefficients $\kappa_\parallel$, $\kappa_\perp$ and $\kappa_\wedge$ can be expressed in terms of the Spitzer-Härm conductivity, κ_e, as

$$\kappa_\parallel = \kappa_e, \quad \kappa_\perp = \kappa_e f_\perp(\Omega_e \tau_{ei}), \quad \kappa_\wedge = \kappa_e f_\wedge(\Omega_e \tau_{ei}),$$

where $f_\perp$, $f_\wedge$ are the functions describing the magnetization of the heat flux. In addition, $\Omega_e \sim |\boldsymbol{B}|$, is the electron cyclotron frequency and τ_{ei} the electron-ion collision frequency. Note that Ω_e has the dimension of the reciprocal of time, thus parameter $\Omega_e \tau_{ei}$ is dimensionless; it describes the effect of the magnetic field on the electron heat conductivity as a ratio between the electron gyration time in the magnetic field and the electron collision time. Bearing this in mind we have displayed in FIG. 4.2 the normalized Braginskii transport coefficients with respect to the normalized parameter $\Omega_e \tau_{ei}$ knowing that $f_\perp(x) = \frac{1}{1+x^2}$, $f_\wedge(x) = \frac{x}{1+x^2}$. For a weak magnetic field, that is, $\Omega_e \tau_{ei} \in [0, 1]$, we have $\kappa_\perp > \kappa_\wedge$, whereas for a strong magnetic filed $\kappa_\perp < \kappa_\wedge$. In the limit $|\boldsymbol{B}| \to 0$, the normalized parameter $\Omega_e \tau_{ei}$ also tends to zero and the Braginskii coefficients behave as follows: $\kappa_\perp \to \kappa_e$ and $\kappa_\wedge \to 0$. In this regime, the anisotropic conductivity tensor K_e recovers the isotropic Spitzer-Härm conductivity, i.e., $\mathsf{K}_e \to \kappa_e \mathsf{I}_2$.

We conclude this section by remarking that K_e is not symmetric and transforms as $\mathsf{K}_e(-b) = \mathsf{K}_e^t(b)$. This non-symmetry of the conductivity tensor is a consequence of the presence of the magnetic field, this behavior is known as the Righi-Leduc effect, refer to [71] chapter XI. It rotates the heat flux vector without changing its absolute value. This property corresponds to the following result: for all arbitrary vector $\boldsymbol{\phi}$

$$\mathsf{K}_e \boldsymbol{\phi} \cdot \boldsymbol{\phi} = \kappa_\perp |\boldsymbol{\phi}|^2.$$
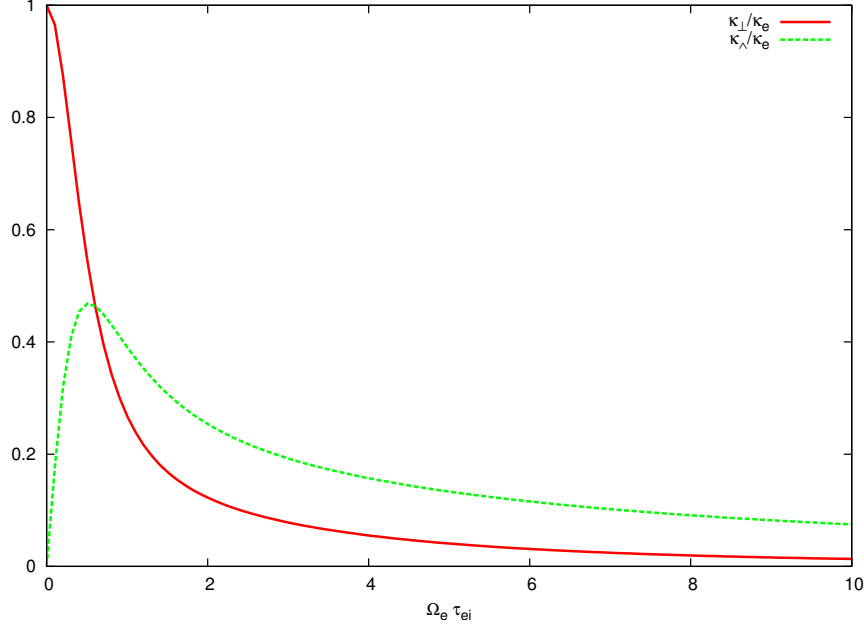
Figure 4.2: Normalized Braginskii transport coefficients $\kappa_\perp$ and $\kappa_\wedge$ versus normalized parameter $\Omega_e \tau_{ei}$.

Since $\kappa_\perp$ is positive, the above result shows that K_e is a positive definite tensor which satisfies the thermodynamic requirement. It is interesting to note that for an arbitrary vector $\boldsymbol{\phi}$, $\mathsf{K}_e \boldsymbol{\phi}$ can be decomposed as follows

$$\mathsf{K}_e \boldsymbol{\phi} = \kappa_\perp \boldsymbol{\phi} + b\kappa_\wedge \mathcal{R}_{\frac{\pi}{2}} \boldsymbol{\phi}, \qquad (4.6)$$

where $\mathcal{R}_{\frac{\pi}{2}}$ denotes the counterclockwise rotation through the angle $\frac{\pi}{2}$. The above equation states that the anisotropic conductivity tensor acts as an isotropic conductivity tensor supplemented by a rotation tensor which follows directly from the magnetic field. Finally, computing the divergence of the anisotropic heat flux (4.3) yields

$$\nabla \cdot \boldsymbol{q}_e = -\nabla \cdot (\kappa_\perp \boldsymbol{\nabla} T_e) + \boldsymbol{A} \cdot \boldsymbol{\nabla} T_e, \qquad (4.7)$$

where $\boldsymbol{A} = [-\frac{\partial}{\partial y}(b\kappa_\wedge), \frac{\partial}{\partial x}(b\kappa_\wedge)]^t$. Under this form the anisotropic diffusion operator appears as the sum of an isotropic diffusion operator plus an advection operator characterized by the velocity-like vector $\boldsymbol{A}$. This decomposition suggests to solve the anisotropic heat conduction equation discretizing separately the isotropic diffusion operator and the advection operator. However, such a splitting strategy may suffer from a lack of robustness in case of strong magnetic fields. That is why, the numerical scheme used in the sequel is based on an anisotropic heat conduction [115].

4.2.2 Magnetic field effects in a 2D configuration

We first test our method on a 2D problem without hydro and a constant and imposed magnetic field :

$$B(x,y) = B_0 \exp^{-\left(\frac{\sqrt{(x-x_0/2)^2 + (y-(1+x_0/2))^2}}{x_0/4} \right)^4} \text{ with } x_0 = 20.10^{-4} \text{ and } B_0 = -1.10^7 G.$$

Our domain is a square of $20 \times 20 \mu m$ with a mesh of 50×50 cells. It is field of Hydrogen $Z = 1$ with a constant initial density of $0.025 g/cm^3$. Initial temperature is $T_1 = 1.10^3 K$

101

for $0. < x < 18.\mu m$ and $T_1 = 3.10^7 K$ for $18.\mu m < x < 20.\mu m$. We run three different types of computation first is Braginskii without Righi-Leduc effect then we have an effective conductivity which is used usually in 2D code then our tensorial formulation (see FIG. 4.3). On the 2D isoline of temperature we can observe a limitation of the heat flux on all the results due to the magnetic field. Then if we take into account of the Righi-Leduc effect with tensorial formulation the rotation of the heat flux is enhanced and no oscillation is observed (FIG. 4.4).
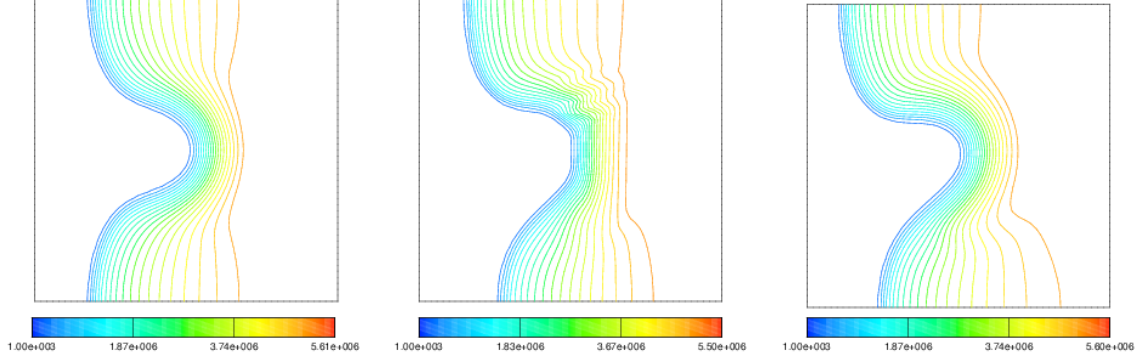
Figure 4.3: Braginskii without Righi-Leduc effect (left), effective conductivity treatment (center), tensorial formulation (right) at $t = 25ps$.
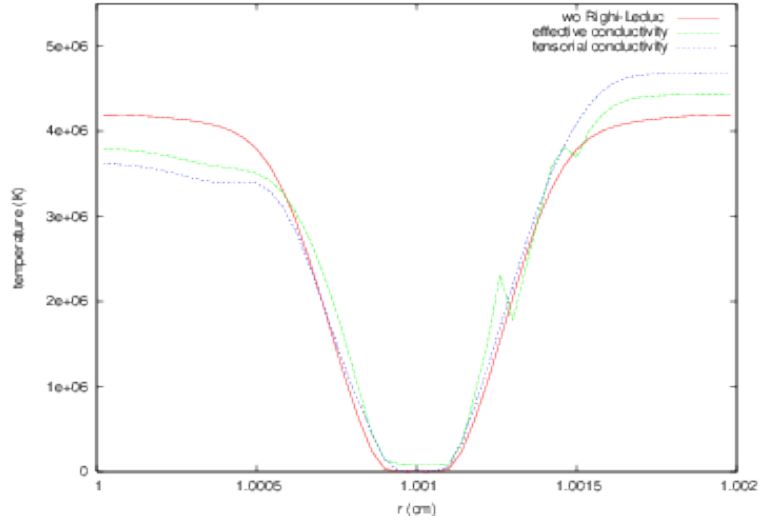
Figure 4.4: Temperature profile at $x = 10\mu m$ and $t = 25ps$.

4.2.3   Plastic target irradiated with a Laser

In this case we study a plastic target (CH) of 100 μm thickness and 1000 μm height irradiated by a laser beam : $\lambda = 0.35$ μm, maximal intensity $1. \, 10^{15}$W cm^{-2}.

This tensorial method leads to a better computation of the Braginskii fluxes. Contrary to the effective method in which the Righi-Leduc effect is partially truncated this tensorial scheme correctly rotates heat fluxes. Comparison between Spitzer and Braginskii show that magnetic field play an important role in the case of laser ablation physics. We can see that magnetic field appear in the zone where density and temperature gradients are not colinear. The magnitude of

the self-generated magnetic field is also more intense using the tensorial method (see Fig. 4.5). The effect of self-generated magnetic field in the case of a laser ablation case totally changes the heat transport process. The tensorial method in this case also presents result free of numerical oscillation.
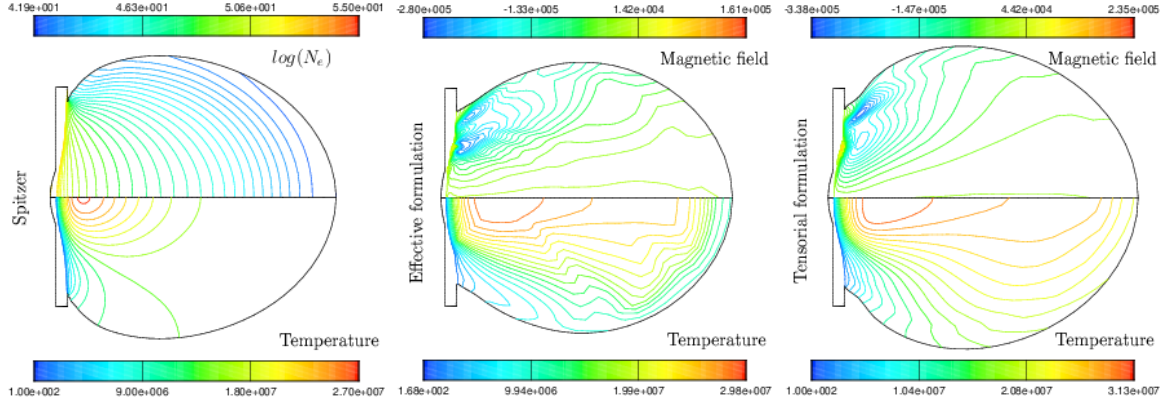

Figure 4.5: temperature and $log(N_e)$ Spitzer (left), temperature and magnetic field effective conductivity (center), temperature and magnetic field tensorial conductivity (right) at $t = 1.25ns$.

4.3 Hydrodynamic implosion symmetry of HiPER's targets

In ICF, within the Fast-Ignition strategy (FI), the use of Petawatt class lasers allows to directly deliver ignition energy to the target. A much less energy is then required by the main laser pulse; ignition being achieved by ultra-fast and ultra-intense ignition laser. First designs show that corresponding implosion velocity is reduced, suggesting that hydrodynamic instabilities could be reduced. First we recall the main features of the laser nonuniformities optimization, within HiPER constraints. Then 2D perturbed simulations as well as a hydrodynamic perturbation modeling sequence are presented.

4.3.1 Irradiation nonuniformities study

Irradiation nonuniformities are directly connected to the laser device. Such nonuniformities produce low mode perturbation which needs to be accurately known in order to investigate the consequence on hydrodynamic target stability. For this purpose a specific illumination 3D code, the CECLAD code, has been developed [63]. It calculates target irradiation by multi-laser beams and enables to optimize illumination of complex geometries in terms of energy distribution in the focal spot or beams number. To improve confidence in CECLAD, the code has been validated against published results [42], with analytical solutions [164] giving perfect uniform irradiation and with existing results of known facilities (Omega). Published results are reproduced. The CECLAD code has been used to define the baseline specifications of the HiPER project (see Appendix C and [60]).

Optimization procedure

Several configurations of laser beams (size, energy balance, pointing, centering) and target (shape, position, size) can be tested with this tool (see Appendix C). The irradiation uniformity can be optimized through various criteria. The first one is the quadratic mean of deviation of
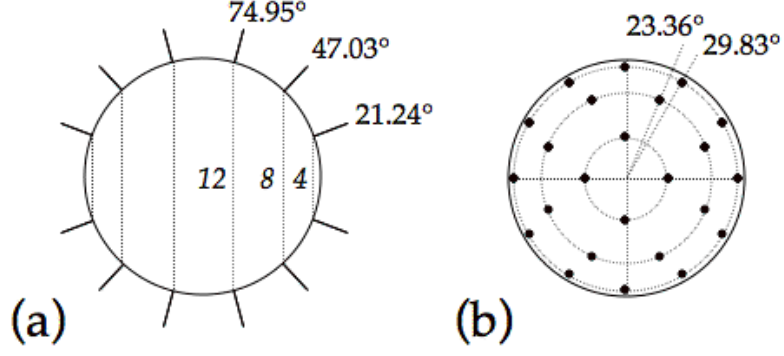
Figure 4.6: The polar (a) and azimuth angles of the 48 illumination scheme.
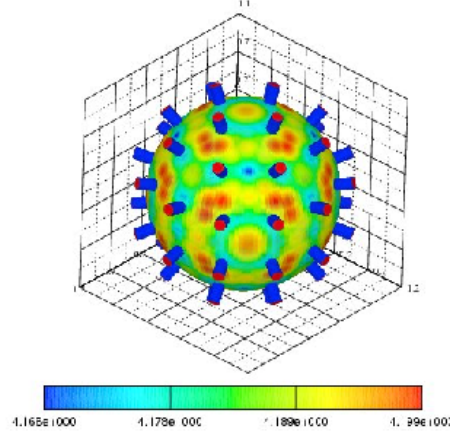

Figure 4.7: Nominal irradiation of the 48 illumination scheme.

the intensity (σ_{rms}) which is a function of parameters featuring beams and targets. The second one is the energy balance η_B which is the ratio between the energy on the target and the laser beam energy. A Legendre polynomial expansion of the illumination gives amplitudes of the main modes. These criteria determine a robustness analysis by varying control parameters of the beams. Statistical variations according to a normal distribution around the nominal configuration can be performed to test the robustness of the chosen pattern.

A 48 beams HiPER illumination scheme

Initial HiPER specifications are 50 beams with 15 kJ per beams at 1 ω (6 kJ at 3 ω) [60]. From these technical constraints one can carry out a σ_{rms} and an energy balance η_B analysis. Obviously the σ_{rms} decreases with the number of laser beams. Meantime the energy balance reaches a value close to 97 % for a 60 laser beams configuration (OMEGA). If one describes the energy distribution in the focal spot by two parameters a, where a is radius at 1/e intensity, and by m, the order of the supergaussian,

$$I(r) = \exp\left[-\left(\frac{r}{a}\right)^{2m}\right],$$

a 48 laser beams scheme described in FIG. 4.6 gives σ_{rms}=0.15 % and $\eta_B = 94\%$ for parameters $a = 0.61$ and $m = 1.02$. On FIG. 4.7 we show a 3D representation of the target with all the beams impinging on it. The field represented on the target is the intensity. This 48 beams
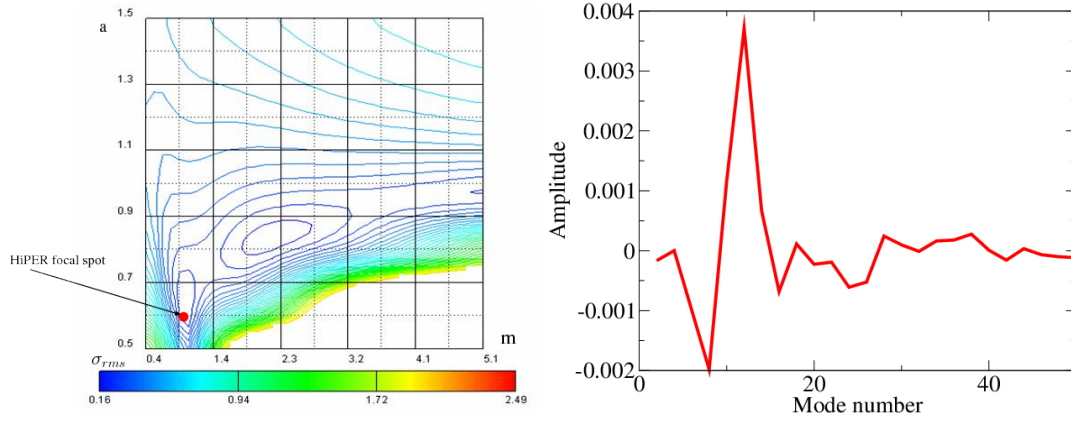
Figure 4.8: On the left σ_{rms} contours in a a, m diagram for the 48 beams HiPER illumination scheme, on the right calculated illumination spectrum (relative amplitude on mode number) for the 48 beams HiPER illumination scheme.

illumination scheme yields small σ_{rms} during the whole target implosion (i.e., a increasing) as it can be seen in FIG. 4.8 which shows σ_{rms} contours in a a, m diagram.

The robustness of this scheme has been tested over 100 000 realizations. A normal repartition of the beam to beam imbalance (10%), of the beam pointing (5%), and of the beam centering 2% have confirmed previous values and given a validity σ_{rms} range. Within the frame of the FI, cone presence can strongly damage illumination uniformities. This 48 beams pattern yields also a low intensity on cone surface and reduces undesired effects like preheating of the cone surface. A Legendre polynomial expansion has been carried out which shows modes related to main illumination nonuniformities are l=12, 8 and 10, with a maximum relative nonuniformity of 0.5 % for mode l=12 (FIG. 4.8 on the right).

4.3.2 Perturbed hydrodynamics simulations and modelings

We want here to show the validity of a linear approximation in the hydrodynamic perturbation growth, and to justify a monomode, half a wavelength, perturbation on a sector type mesh. Two sets of simulations have been carried out on the Atzeni's design [11] which is considered here as the reference test case for the hydrodynamic perturbation modeling sequence.

The full spectrum of the laser irradiation has been introduced in the 2D CHIC [33] simulations on a 90 degrees mesh grid. Strictly speaking only even modes can be dealt with because of the mesh symmetry. The mesh includes 256 grid points in the radial direction, with a refinement in the absorption region, and 56 grid points, regularly spaced, in the transverse direction. The mode number l=20 will be described by 6 grid points for half a wavelength which limits our multimode analysis to mode numbers lower than 20. For simplicity reasons, laser power has been calculated from 1D total absorption at the critical density and modulated by a Legendre expansion, constant in time, taken from FIG. 4.8 (on the right). The resulting illumination versus angle is presented in FIG. 4.9.

Multimode CHIC (FIG. 4.10) simulation indicates that the mode number l=12 remains dominant up to the time of maximum areal density, i.e., the stagnation time. The maximum deformation achieved at internal interface is about 10 μm from peak to valley. This deformation is the consequence of the illumination nonuniformities which have seeded perturbations at the ablation surface. Then these perturbations have been transmitted to internal interface during shock wave transit and amplified by Bell-Plesset mechanism. Fourier analysis, i.e., modal analysis, of the internal interface deformation at stagnation is presented in FIG. 4.11. It confirms
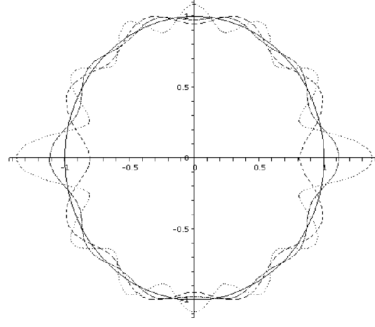
Figure 4.9: Illumination spectrum versus angle applied in 2D multimode CHIC simulations. The mode number l=12 is the dominant mode number.
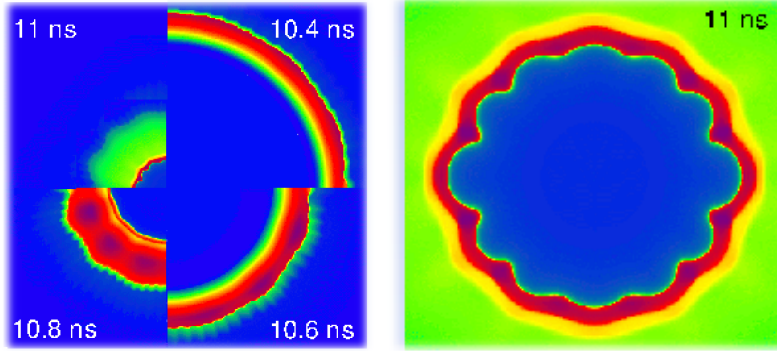

Figure 4.10: Multimode, 90 degrees, CHIC simulation of Atzeni's reference design. Four density contours at time t=10.4 ns, t=10.6 ns, t=10.8 ns and t=11 ns are presented on the left panel. A magnified view of density contours is presented on the right panel at time t=11 ns, i.e., just before time of maximum areal density ($\approx$ 11.17 ns).

that dominant mode number is the l=12 and it shows that lower mode numbers have considerably decreased. Nonlinear mode coupling does not really take place, although contribution of l=16 mode number slightly increases. This result is confirmed by an evaluation of the ratio perturbation amplitude on inflight radius ($a/\Delta R$) which is lower than 1 (not shown here). These results show that deformation of the internal interface can be obtained with monomode simulations, the whole spectrum being obtained by reconstruction of each modal contribution. Moreover, previous studies [80] have shown that monomode simulations by using sector grid meshes covering half a wavelength gave results similar to that obtained on a 90 degrees mesh.

4.4 Non-linear amplification of high mode perturbations at ablation front in HiPER targets

A safety factor discussion for low modes perturbations ($l \leq 50$), related to laser irradiation non uniformities, is addressed in Ref. [74]. It is shown that a self-consistent numerical method provides accurate estimates for the perturbation growth at the ablation front and at Deuterium Tritium (DT) interfaces. Also some analytical estimates could be obtained by coupling the perturbed shock waves with the ablation front in a high aspect ratio target. Thus, the perturbation growth can be understood by combining direct numerical simulations with a model post-treatment for low mode numbers corresponding to large wavelength perturbations. These
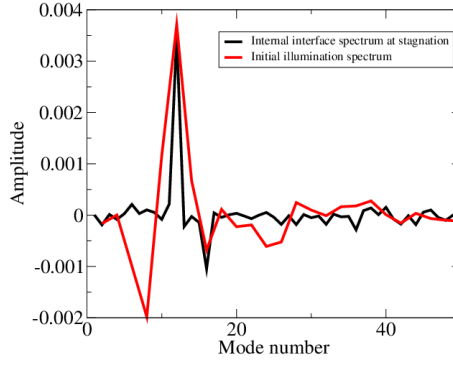
Figure 4.11: Fourier analysis, i.e., modal analysis, of the internal interface deformation at stagnation. The mode number l=12 remains the dominant mode number which justifies linear monomode simulations in order to study the deformations up to the stagnation phase.

perturbations can be initiated, for example, by laser irradiation non uniformities. A tolerance guideline on the laser irradiation was suggested and dominant mode numbers were identified.

Pursuing hydrodynamic stability studies for the HiPER baseline target, we address here the problem of high mode perturbations ($l \geq 20$) induced by shell roughness.

Here, contrary to the low wave numbers case, non-linear behaviour has to be accounted for during the shell acceleration. Finally, it is shown that, for high modes, the ablative Rayleigh-Taylor (ART) instability behaves apart from the spatial perturbation seeded during the shock transit time. It depends only on the amplitude achieved at the beginning of the acceleration. Numerical simulations with 2D code CHIC [33] provide an accurate estimate of the linear perturbation growth and give an assessment of the non linear stage. It is also shown that stabilizing schemes based on adiabat shaping [8] reduce the perturbation growth and delay the beginning of the non-linear phase. This allows to discuss the problem of determining the admissible initial roughness spectrum for the baseline HiPER target. A good agreement is found between simulations and self-consistent theories up to the end of the weakly non-linear phase.

4.4.1 Non-linear ART simulation with the ALE CHIC code

To study the perturbation evolution at the ablation front we impose a Legendre single-mode perturbation at the external surface. This perturbation is radial and, because of the relatively small range of the spatial perturbation dependency, a linear decay inside the shell is used. This approximation preserves the ART seeding and growth. A purely Lagrangian computation may stop before end of acceleration, during the non-linear stage due to tangled mesh. The ALE method allows to improve the geometrical quality of the grid elements and to optimize accuracy, robustness, and computational efficiency. A special rezoning procedure is implemented in the ablation zone. A traditional mesh smoothing is not sufficient in our case as it could decrease the accuracy of the Lagrangian computation with the consequence to loose the spatial resolution. It is necessary to preserve the Lagrangian displacement at the ablation front. In the rezoning procedure implemented in CHIC, the Lagrangian characteristic of the mainstream flow and especially the perturbation at the ablation front are preserved using an orthoradial projection. In this rezoning procedure we keep the radial Lagrangian displacement of the nodes during all the computation and we orthogonally project the orthoradial displacement onto this radius. The rezoning phase is followed by a second order remapping phase where all the conservative quantities are conservatively remapped from the Lagrangian mesh onto this rezoned mesh. Once the non-linear perturbation growth has started, we add to this rezoning an additional
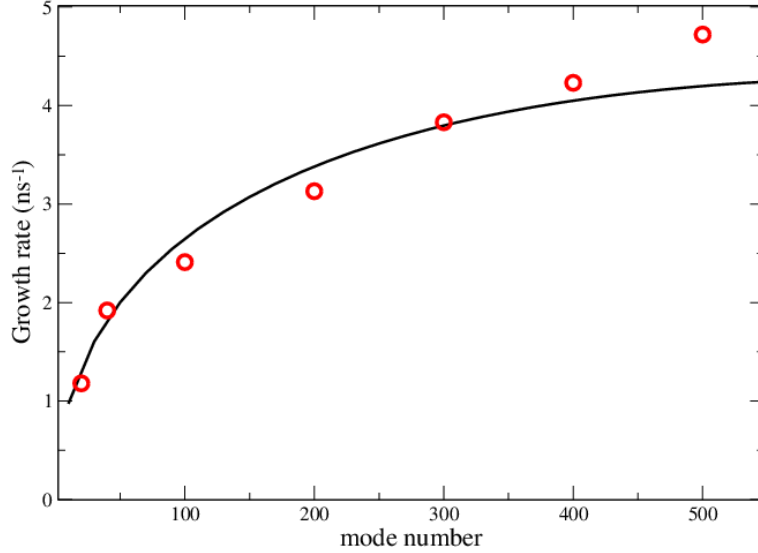
107

Figure 4.12: Linear growth rate at short times (7.5 - 8 ns) versus mode number obtained from the CHIC simulations (dots) compared to theoretical model (solid line) [25].

mesh smoothing to avoid mesh tangling. By using such rezoning, a non-linear evolution of mode numbers up to $l = 800$ can be studied by using 35 grid points per wavelength.

4.4.2 2D high mode simulations of perturbed flow

FIG. 4.12 presents a cross-check validation of high mode instantaneous linear growth rates obtained in CHIC simulations and from theory [25]. This comparison is made for short times up to 8 ns, because of the early non-linear stage, which occurs for modes higher than l=100 including small initial perturbation amplitudes. Indeed for $l = 100$ and a 0.1 cm radius, the non-linear threshold $ak \sim 0.1$ [96] is expected to be reached, for amplitudes larger than 1 μm, in the nanosecond time scale. Note that at the beginning of acceleration, most unstable modes are in the range [500-600] as the maximum growth factor are obtained for modes in the range [200-300]. It shows an important time dependency in the perturbations development for the linear and non-linear regimes, including the contribution of at least the second harmonic.

In FIG. 4.13(a) we show the perturbation amplitude at ablation front versus time for different initial amplitudes with initial single-mode perturbation $l = 200$. The transition to the non-linear stage is indicated by the slope modification in the amplitude evolution. The perturbation evolves in the linear regime (see FIG. 4.13(b)) and then reaches the weakly non-linear regime (FIG. 4.13(c)). At that moment, the particular shape of density contours are characteristic of the ART instability behaviour. Here at least a double frequency structure is present. The effect of ablation on the perturbation shape during the weakly non-linear regime is clearly seen. This shape is described and explained in [144, 143]. The spikes may flatten and enlarge due to the dynamical ablation overpressure. In this regime, the perturbation shape is the result of early seeding of harmonics and their feedback to the fundamental mode. These harmonics can appear with the same or opposite phase relatively to the fundamental mode [144]. FIG. 4.14 (a) shows the amplitudes (absolute values) of the first and second harmonics as a function of time. FIG. 4.14 (b) shows a Fourier analysis of the modal spectrum during the main acceleration, at time t=9.2 ns, up to fifth harmonic. The density contours shape (wide and flattened) in FIG. 4.13(c) is due to the phase inversion of the second harmonic (FIG. 4.14 (b)).

The different shapes of the density contours for $l = 200$ are shown at different times in FIG. 4.15
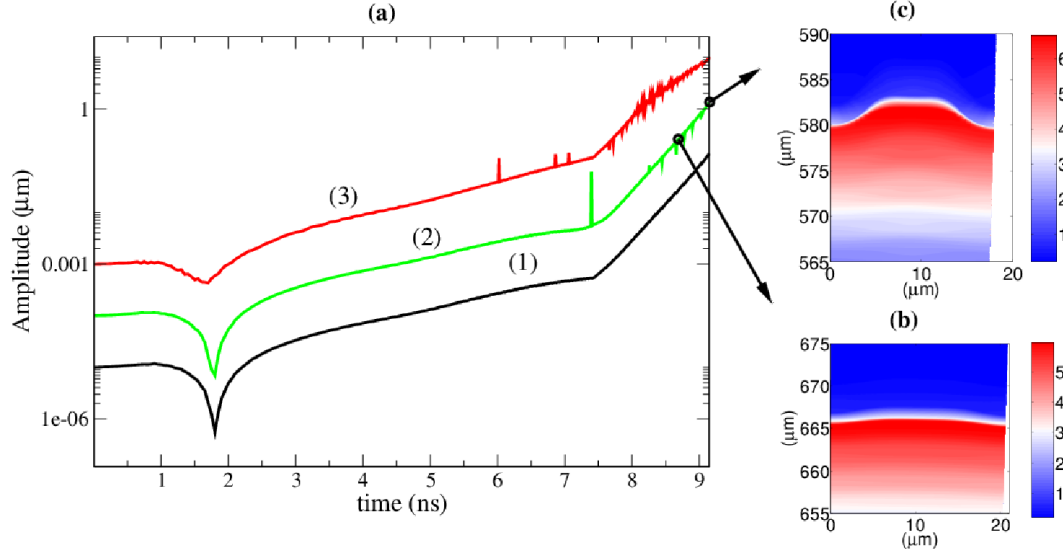
108

Figure 4.13: a) Ablation front perturbation versus time for $l = 200$ mode with three different initial amplitudes and density contour shapes (g/cm^3) of curve (2) at times b) 8.7 ns and c) 9.2 ns. On density contours, the blue zone on the top is the external vacuum, the red zone is the compressed DT and the blue zone on the bottom is the vapor-pressure DT gas in the center.

excited by the initial roughness of about 1 nm (FIG. 4.15a-b-c). A peak-and-valley shape can be seen up to the fully non-linear regime at the time t > 9 ns. The non-linear shape consists in spikes and bubbles structures. At the end of the simulation, multi-frequency structures appear. For a few nm initial amplitude, the non-linear evolution lasts most of the acceleration phase and non-linear couplings may be very strong. For a higher initial amplitude around 10 nm and more, characteristic structures appears with very singular shape (see FIG. 4.15 (e)), previously observed in planar simulations in [144]. At large time, an asymptotic case is achieved, where the shell is completely decompressed (FIG. 4.15 (f)). These initial conditions lead to exhibit very complex multimode structures of the non-linear regime, where ablation plays an important role. Namely the shape of the perturbation differs from the classical case where thin spikes and thick bubbles are expected [144]. This new repartition is clearly observed for higher modes in our simulations. In FIG. 4.16, for mode $l = 300$, one can see the clear inversion of the shape perturbation (thin bubbles, thick spikes) from the weakly non-linear stage (FIG. 4.16(a)). This behaviour has been observed for all higher modes. Theory exhibits a threshold wave number for this feedback. Our simulations, initiated by a single-mode perturbation ($l = 300, 500, 800$), reproduce the inversion of spikes and bubbles thickness, contrary to a classical Rayleigh-Taylor (RT) weakly non-linear perturbation shape, i.e., without ablation. Simulations results are consistent with the existence of this threshold and all unsteady effects. For example, the dominant mode in the linear regime differs at the beginning of the main acceleration and subsequent times. For this reason, the non-steady effects act on the growth of both fundamental and harmonics of the initial perturbation. The initial amplitude may also change the contribution of the behaviour corresponding to each mode perturbation. At later times, the perturbation evolves in the non-linear regime with a multimode bubble-spike structure (FIG. 4.16(b)). Non-linear effects at the ablation front produce very elongated bubbles which extend from the ablation front into the expanding low density plasma (FIG. 4.16(c)).

Figure 4.17 shows the temporal evolution of the perturbation amplitude at the ablation front for the mode $l = 300$ and for three initial amplitudes. The behaviour is the same before the main acceleration phase as long as the perturbation remains in the linear stage. The slope
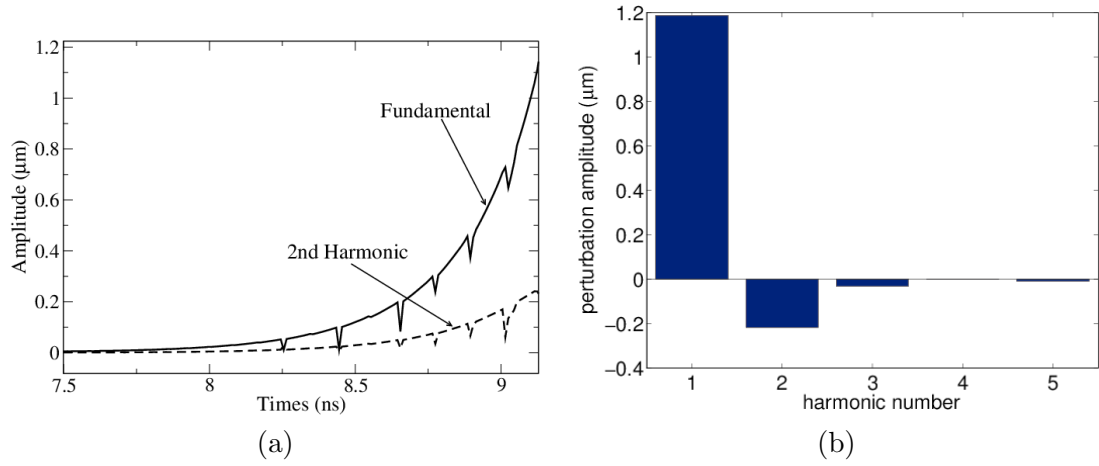
Figure 4.14: For mode $l = 200$: a) Amplitude of the first and second harmonics versus the time during the acceleration phase; b) Fourier analysis of ablation front perturbation at time 9.2 ns acceleration, up to fifth harmonic. The second harmonic appears with opposite phase.

variation indicating the non-linear perturbation behaviour occurs for the same amplitudes. The Y curves indicate fraction levels of the perturbation wavelength λ. In particular, $Y = 0.1\lambda$ corresponds to the classical weakly non-linear saturation criteria [96]. For the mode $l = 300$, we checked that the radiation transport has weak influence on the instability growth. At the end of acceleration, the radiation changes the amplitude less than 10%. For modes greater than 300, the shape inversion was observed, with thicker spikes. Additionally, for these modes, the perturbation may reverse phase during the weakly non-linear stage. A multimode computation has been also performed FIG. 4.18 based on a initial $l = 300$ and with 10% of $l = 100$. It exhibit bubble competition and indicate that a study should be performed using real initial spectrum for the baseline HiPER target, has performed in the work of [130]. Experimental study has also been realized to study the ART instability growth [52], on the OMEGA laser facility and the radiation hydrodynamic CHIC code has been used for the design and the interpretation of the results.
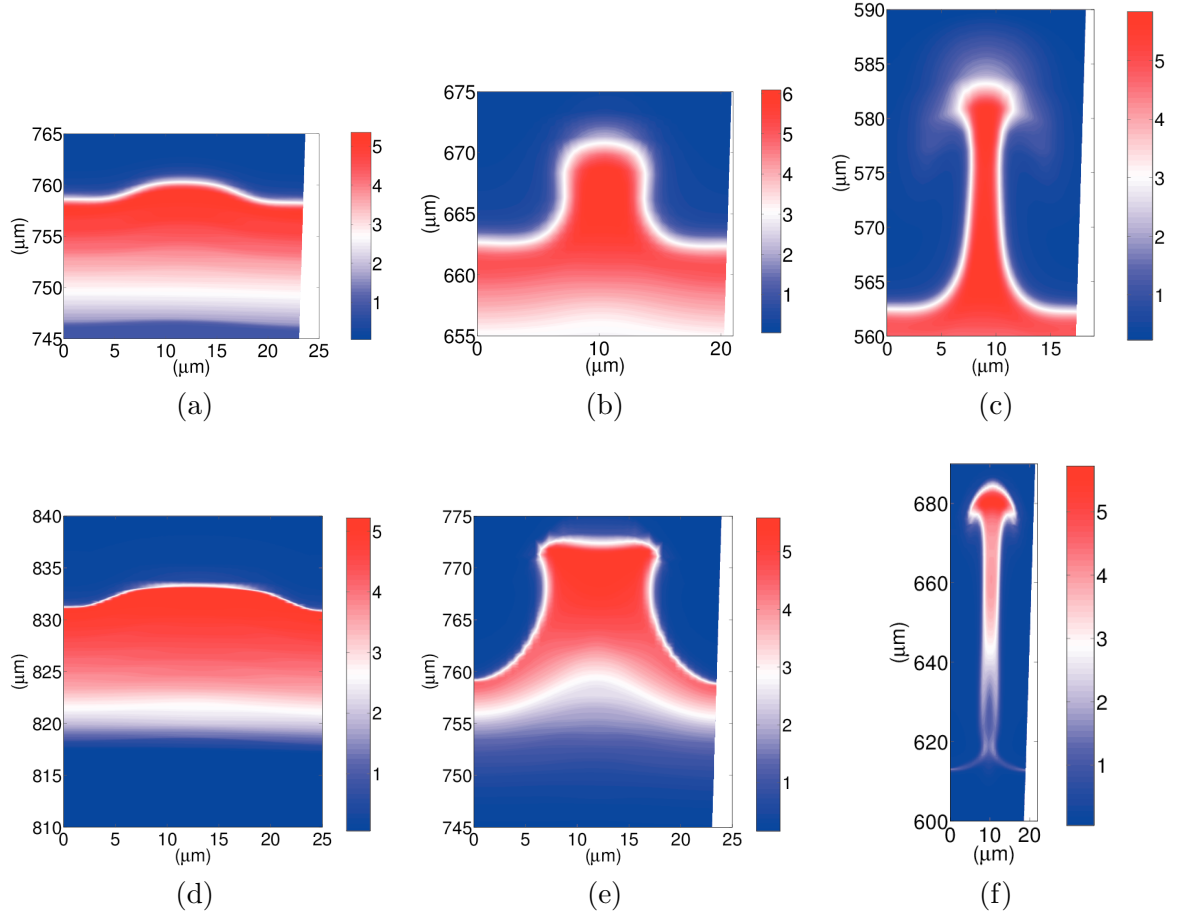
Figure 4.15: Evolution of the perturbation shape on density contours for $l = 200$ mode: with initial amplitude $a_0 \sim 1$ nm at times a) 8 ns, b) 8.7 ns, c) 9.2 ns; with initial amplitude $a_0 \sim 10$ nm at times d) 7.3 ns, e) 8 ns, f) 8.7 ns. On density contours, the blue zone on the top is the external vacuum, the red zone is the compressed DT and the blue zone on the bottom is the vapor-pressure DT gas in the center.
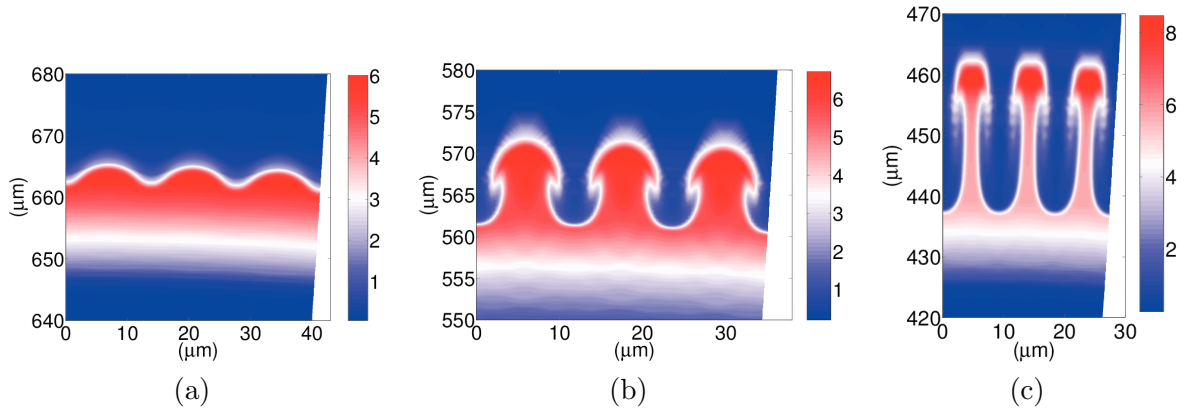

Figure 4.16: Evolution of the density contours of mode $l = 300$ at times a) 8.7 ns, b) 9.2 ns, c) 9.7 ns. An inversion of the bubble-spike symmetry is observed.
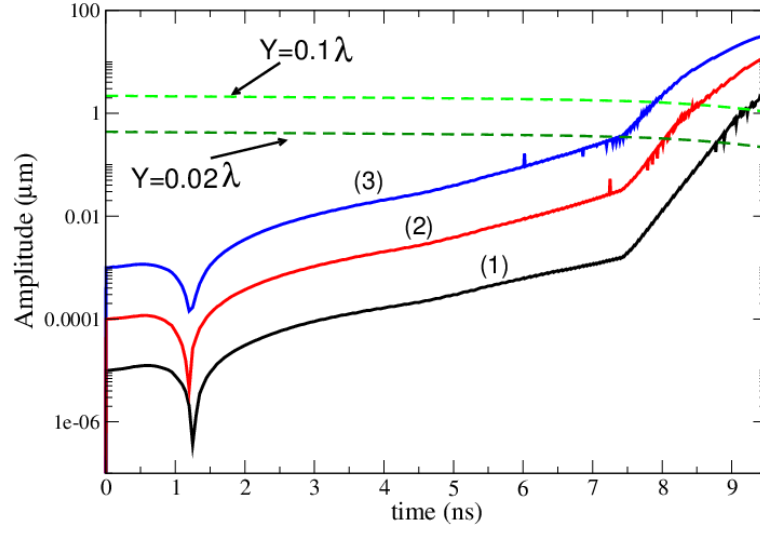
111

Figure 4.17: Ablation front perturbation amplitude versus time for $l = 300$ mode, with standard pulse and three different initial amplitudes.
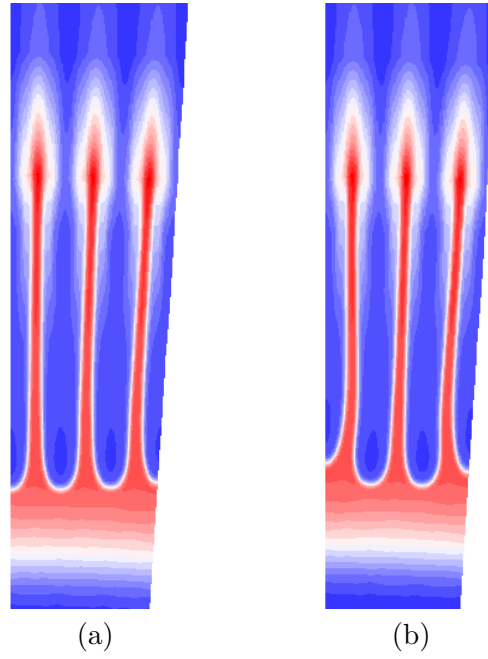

Figure 4.18: a) Monomode calculation $l = 300$; b) multimode for $l = 300$ and 10% of $l = 100$ both at time t=10.2 ns.

4.5 Study on shock propagation in the context of polar direct drive shock ignition

In the Direct-Drive Inertial Confinement Fusion (ICF) scheme, the classical process leading to DT ignition is the conversion of the shell kinetic energy into internal energy of a central hot spot, which further acts as an ignition spark [13]. To achieve central ignition, the shock ignition (SI) scheme has been extensively studied theoretically and experimentally [97, 26, 43, 138]. Shock ignition was first proposed by Betti et al. [10], it consist to ignite the target by means of a strong convergent shock launched in the target at the end of the compression phase and prior to the final stagnation of fuel at target center. This new concept has been experimentally studied in planar [138, 20, 10] or in spherical geometry [18, 137, 153]. It was demonstrated that a properly timed final shock significantly enhances the neutron yield [12] and that the coupling of high-intensity spike beam energy into the imploding capsule was studied, which suggests that the yield increase was partially due to hot electrons coupled into the compressing target. [79]. Recently, encouraged results obtained from strong spherical shock [152] demonstrate the capability to generate high shock pressure 300 Mbar at laser intensities in the range of 1015 to 1016 $W/cm2$. This physical issue is crucial for the credibility of SI [152].

In this section, we study the possibility to ignite the hot spot with a strong no-uniform irradiation for the ignitor shock. The shock ignition is a two step process, first a uniform illumination compressed the target at low velocity, then a strong shock converge to ignite the hot spot. Although the compression require a uniform irradiation, for the ignitor shock it is not mandatory require. This possibility studied in [153] shows that because the critical radius target is reduced at the shock launching time, the focal spot needed for the ignitor could be smaller than the compression beam. This allow a better absorption and demonstrated the high flexibility and robustness of this concept [153], i.e. even in bipolar irradiation the ignition occurs. In this configuration the hydrodynamic simulations show that two planar shocks propagate inside the hot spot and collide to ignite the target. To study the bipolar ignition scheme, an experiment on the LIL facility was proposed to experimentally reproduce the formation of a convergent planar shock by a spike laser pulse in presence of a SI relevant plasma. In this experiment, the LIL quad Gaussian beam is focused on hemispherical target and compare to the planar one. In the two configurations VISAR an SOP diagnostics allowed to give to the inferred shock pressures and shapes.

Here we report the results obtained on the hemispherical target. Due to the complex geometry this experiment was the first which use the multi-material Eulerian version of CHIC at CELIA. This version uses the last development of the CHIC code for the multi-material treatment based on the MOF method for the interface reconstruction. As it is shown in FIG. 4.19 and FIG. 4.20 the CHIC code enables to recover all the shock timing at ± 100 ps visible on the VISAR diagnostic.

The initial configuration is shown in FIG. 4.20(a) on the left and right very light density material also called pseudo material are initialized. Then from the left to the right we have a thick slice of quartz of $250 \mu m$, then $30 \mu m$ of Molybdenum (Mo) and finally the CH part of the target which include the hemisphere. At $t = 2.4ns$, FIG. 4.20(b), the shock as penetrated the Mo and it is the first signal visible on the VISAR FIG. 4.19. At this time the pseudo material on the right has been totally replaced by the CH plasma due to the ablation of the CH target. At $t = 3.7ns$, FIG. 4.20(c), a planar shock reach the left interface of the Mo and it corresponds to the plateau of FIG. 4.19. At that time we can see the thin Mo slice has been compressed by the shock. At $t = 7.1ns$, FIG. 4.20(d), a shock reach the left interface of the quartz which is visible on FIG. 4.19. Here the Mo is much deformed by the shock interaction. At $t = 12.25ns$, FIG. 4.20(e), two shock converge on the left interface of the quartz and change the slope of
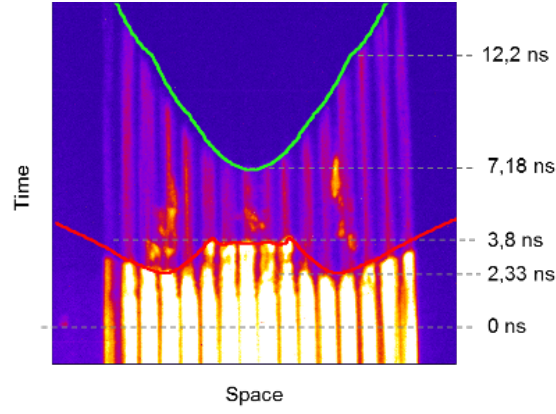
Figure 4.19: VISAR experimental results compared to the simulated VISAR using the CHIC code (red and green curve).

the VISAR results, green curve on FIG. 4.19. As the laser has been turned off at $t = 4ns$ the Mo expand and some droplet of material are visible on FIG. 4.20(e) and FIG. 4.20(f). The quartz penetrate the pseudo vacuum on the left. Due to the very strong deformation of the Mo material on FIG. 4.20(f) we can see that some cells contain three different materials quartz-Mo-CH which is one of capability of the MOF method to track multi-material cell with more than two materials.
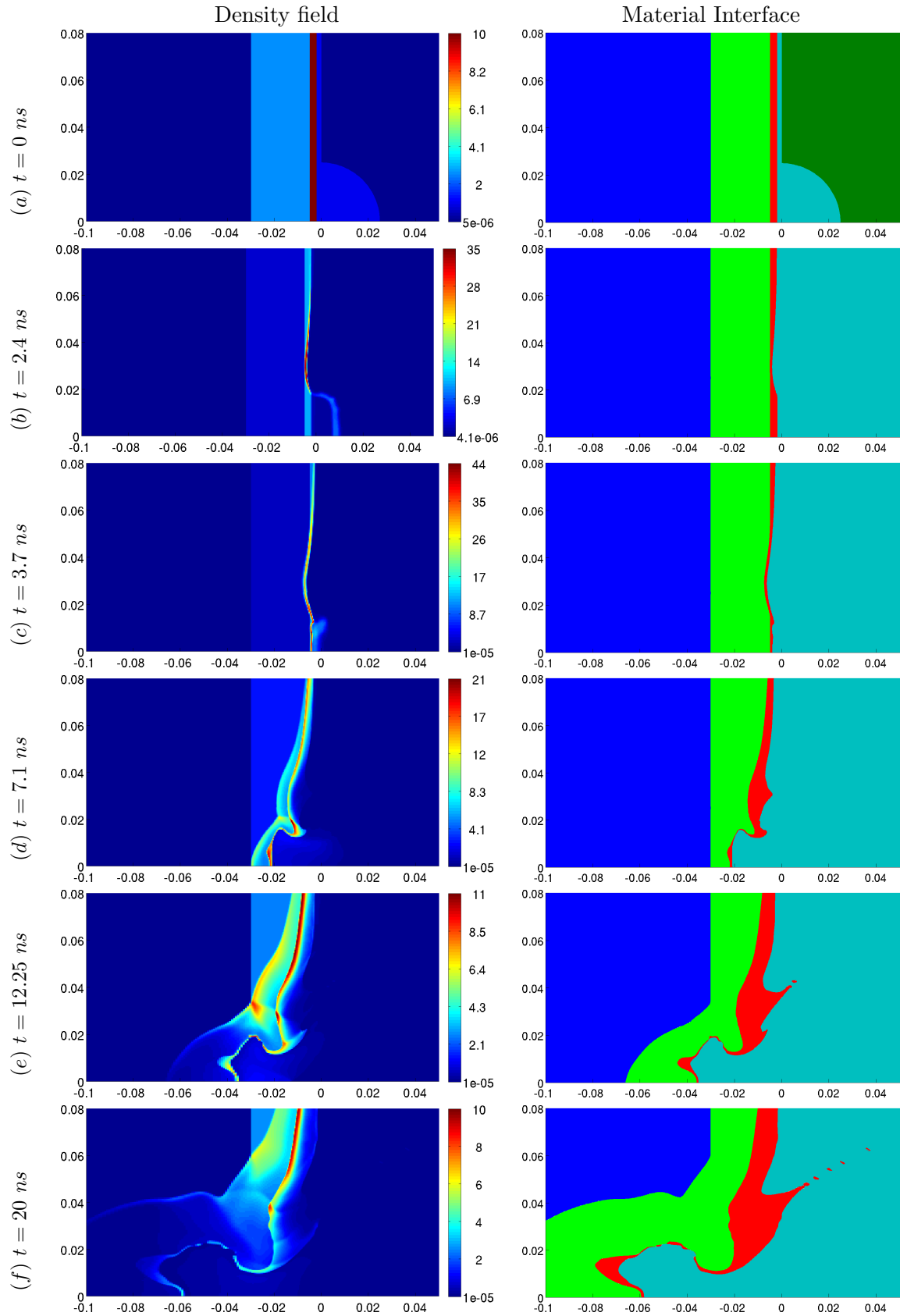
Figure 4.20: Density fields (left) and material interface (right) at different time.

115